JGR Solid Earth

Key Points:
- A published velocity model derived from surface wave inversion is used to constrain the 3-D magnetotelluric inversion at Laguna del Maule
- Discrepancies between the velocity and resistivity models are likely due to magma storage conditions rather than inversion nonuniqueness
- The MT images a crystal-poor melt volume within a larger crystal-rich mush imaged by seismic indicating a thermally heterogeneous system

Integrating Magnetotelluric and Seismic Images of Silicic Magma Systems: A Case Study From the Laguna del Maule Volcanic Field, Central Chile

Darcy Cordell[1] (ID), Martyn J. Unsworth[1], Benjamin Lee[1] (ID), Daniel Díaz[2], Ninfa L. Bennington[3,4] (ID), and Clifford H. Thurber[3] (ID)

[1]Department of Physics, University of Alberta, Edmonton, Canada, [2]Departamento de Geofisica, Universidad de Chile, Santiago, Chile, [3]Department of Geoscience, University of Wisconsin-Madison, Madison, WI, USA, [4]U.S. Geological Survey, Hawaiian Volcano Observatory, Hilo, HI, USA

Abstract Imaging silicic systems using geophysics is challenging because many interrelated factors (e.g., temperature, melt fraction, melt composition, geometry) can contribute to the measured geophysical anomaly. Joint interpretation of models from multiple geophysical methods can better constrain interpretations of the subsurface structure. Previously published resistivity and shear wave velocity (Vs) models, derived separately from magnetotelluric (MT) and surface wave seismic data, respectively, have been used to model the restless Laguna del Maule Volcanic Field, central Chile. The Vs model contains a 450 km^3 low-velocity zone (LVZ) interpreted as a region with an average melt fraction of 5–6%. The resistivity model contains a conductor (C3) interpreted as a region with a melt fraction >35%. The spatial extents of the LVZ and C3 overlap, but the geometries and interpretations of these features are different. To resolve these discrepancies, this study investigates the resolution of the MT data using hypothesis testing and constrained MT inversions. It is shown that the MT data are best fit with discrete conductors embedded within the larger LVZ. The differences between the MT and seismic models reflect resolution differences between the two data sets as well as varying sensitivities to physical properties. The MT data are sensitive to smaller volumes of extractable mush that contain well-connected crystal-poor melt (C3). The seismic data have lower spatial resolution but image the full extent of the poorly connected crystal-rich magma storage system. The combined images suggest that the LdMVF magma plumbing system is thermally heterogeneous with coexisting zones of warm and cold storage.

1. Introduction

Using geophysical data to determine the composition and structure of the Earth is limited by nonuniqueness. This arises in two distinct parts of the data analysis. The first arises in solving a geophysical inverse problem to determine a geophysical parameter (e.g., electrical conductivity, density, or seismic velocity) which fits a set of measured geophysical data (e.g., magnetotelluric, gravity, or seismic data) within some threshold or error level. This nonuniqueness in the inversion arises because (a) measured data are noisy; (b) the problem is underdetermined (i.e., there are more model parameters than data points); and (c) there are often limitations of the inherent physics of the geophysical method (Parker, 1994). A second type of nonuniqueness arises in the geological interpretation of a geophysical model. Interpretational nonuniqueness arises because a particular geophysical parameter can be explained by many combinations of rock composition, temperature, pressure, porosity, etc. (e.g., Lees, 2007; Pommier, 2014; Unsworth & Rondenay, 2013), and because the full complexity of the subsurface cannot be captured by model discretization (e.g., Miensopust, 2017). In light of both inversion nonuniqueness and interpretational nonuniqueness, it is necessary to determine the most reliable geological interpretation by fully exploring the solution space (i.e., the complete range of acceptable models) and quantifying how small changes to the geophysical model impact the data response (i.e., data sensitivity).

These two aspects of nonuniqueness are especially important when geophysical methods are applied in volcanology to investigate the size, location, and composition of crustal magma reservoirs. This is because magma plumbing systems can be comprised of multiphase systems with complex structural geometry. Determining the size, location, and composition of the magma plumbing system has important

implications about the size of future eruptions, eruptive frequency, magma viscosity, and stability of a given volcano (Pritchard & Gregg, 2016). Geophysical studies of volcanos were first reviewed by Iyer (1984) and many subsequent studies have used a variety of geophysical methods (see Magee et al., 2018; and Schmandt et al., 2019, for reviews).

For magnetotelluric (MT) studies, which image the electrical conductivity of the subsurface, these two types of nonuniqueness are relevant at silicic systems because silicic partial melt is not necessarily electrically conductive. The resistivity of a partial melt is dependent on many interrelated parameters including melt fraction, temperature, chemical composition, and water content (e.g., Guo et al., 2016). Silicic systems have relatively low solidus temperatures compared to intermediate or mafic systems, which means that the temperature can be relatively low and silicic partial melts can be stored at low melt fractions (Sparks et al., 2019). Low temperature and low melt fraction partial melts will be much more resistive than high temperature and high melt fraction melts with identical water content, making them difficult to image with MT. Lower concentrations of dissolved water in the magma will also make the partial melt less conductive. Furthermore, magma plumbing systems may be coupled to hydrothermal systems which consist of thin lenses or reservoirs of conductive saline fluids (Afanasyev et al., 2018) or hydrothermal fluids which are volumetrically distributed. Thus, it can be difficult to determine whether a conductor is caused by a zone of partial melt or hydrothermal fluid. In reality, it may often be the case that both of these phases (partial melt and hydrothermal fluids) coexist in the subsurface (e.g., Laumonier et al., 2017; Sanders et al., 1995). Similar issues of nonuniqueness occur in the interpretation of seismic studies of magmatic systems. The geometry, crystal structure, and lithology of partial melt and the surrounding rock can result in subsurface seismic velocity values of similar amplitude to subsurface regions under elevated subsolidus temperatures (Lees, 2007).

The internal structure of magma plumbing systems may consist of thin, high melt fraction dykes and sills or larger, more homogeneous low melt fraction reservoirs. It is unclear that application of MT or seismic methods alone can distinguish between these two end members given their respective resolution limitations (Lees, 2007; Lowenstern et al., 2017).

To produce a more unique interpretation of the magma plumbing system, information from multiple geophysical methods and petrological data are combined. Recently, several volcanos have been investigated with multiple geophysical methods such as MT, seismic tomography, and gravity measurements (e.g., Árnason et al., 2007; García-Yeguas et al., 2017; Pritchard et al., 2018). These methods are sensitive to electrical resistivity, elastic seismic velocity, and density, respectively. In general, partial melt has a low resistivity, low velocity, and low density so it is expected that geophysical inverse models of each parameter will include features which correlate spatially and that interpretations would be congruous (Unsworth & Rondenay, 2013). In some cases, the anomalies imaged by the various methods agree relatively well in terms of location, size, and interpreted composition (e.g., Comeau et al., 2016; Hill et al., 2009; McGary et al., 2014; Ogawa et al., 2014). However, in other cases, there is a discrepancy between the spatial location of anomalies (or the lack of anomalies) determined by the different methods and/or the interpretations from different methods (e.g., Jiracek et al., 1983; Kelbert et al., 2012; Piña-Varas et al., 2018; Stanley & Blakely, 1995).

Discrepancies between different geophysical methods may be due to some combination of differences in resolution between methods, differences in the distribution of measurement locations, and/or differences in how a geophysically determined parameter constrains the rock properties (e.g., electrical resistivity is primarily controlled by a connected network of material whereas seismic velocity depends on bulk properties of the rock). In this way, a discrepancy between several different methods does not necessarily imply a failure of any (or all) methods but instead may provide important additional constraints on the interpretation and thus reduce nonuniqueness (e.g., Cook & Jones, 1995). Therefore, it is important to assess whether discrepancies between the methods are consistent within the uncertainty of the data. In this paper, two types of discrepancies are addressed:

a. A real discrepancy is one where different geophysical methods are sensitive to real differences in subsurface geology within the uncertainties of the measurements. In this case the discrepancy provides additional information about the subsurface structure. For example, Comeau et al. (2016) found that discrepancies in the depth estimate of the Altiplano Puna Magma Body from seismic and MT data were best explained by a layered magma chamber.

b. An apparent discrepancy is one where the differences are due solely to nonuniqueness in the inversion, subject to the data uncertainties, and a congruous model is possible and preferred. For example, Piña-Varas et al. (2018) noted that the lack of an MT anomaly at three hypothesized magma reservoirs on Tenerife could be explained by a lack of resolution in the measured data, rather than requiring a geological explanation.

To investigate model nonuniqueness and data sensitivity in the MT inverse modeling, sensitivity analysis and hypothesis testing are carried out. Sensitivity analysis describes the overall sensitivity of the model (e.g., the Jacobian matrix, Kalscheuer et al., 2010; Muñoz & Rath, 2006; Monte Carlo or boot-strapping methods, Schnaidt & Heinson, 2015; or extremal bounds analysis, Meju, 2009). These methods, while useful, are often computationally expensive and difficult to implement. They also provide a general sensitivity of a model rather than testing whether specific model features are interpretable, or whether specific hypothesized geological features could go undetected. In contrast, hypothesis testing uses forward modeling and constrained inversions to test the sensitivity of specific model features (e.g., Bedrosian, 2007). This is often done by adding a specific feature to a model (i.e., perturbing an existing model) and either computing the data response of the perturbed model or running an inversion with the perturbation as an additional *a priori* constraint. If discrepancies exist between seismic velocity and resistivity models in a particular region, then hypothesis testing can be used to test whether these discrepancies are real or apparent. It is important to mention that different data sets can be combined via joint inversion. These methods do not explicitly test sensitivity or nonuniqueness but provide a way to examine the model (or set of models) which best fits both data sets. Joint inversion methods are often computationally expensive, difficult to implement, and have a variety of additional complexities beyond the scope of this paper (Moorkamp, 2017).

In this paper, the nonuniqueness and data sensitivity of three-dimensional (3-D) MT inverse models is examined by using results from surface wave seismic modeling as a constraint for a variety of hypothesis tests. The Laguna del Maule Volcanic Field (LdMVF) in central Chile (Figure 1) is used as a case study because it is an exceptional natural laboratory with a high concentration of recent rhyolite eruptions (Andersen et al., 2017; Hildreth et al., 2010), recent seismic swarms (Cardona et al., 2018), and ongoing upward ground deformation (Le Mével et al., 2015). The center of observed upward ground deformation (i.e., the inflation center) is located on the southwest side of the eponymous Laguna del Maule (Figure 1). The LdMVF system is in a transtensional regime and faulting appears to play an important role in magma and fluid transport and/or storage (Peterson et al., 2020; Zhan et al., 2019). MT and seismic surface wave and ambient noise data have been collected concurrently at the LdMVF and were used to obtain previously published resistivity and seismic velocity models (Cordell et al., 2018; Wespestad et al., 2019). The resistivity model is investigated by using the seismic velocity model as a constraint to better describe the magma plumbing structure, which can give insight into the stability and future eruptive activity of the system.

2. Methodology

2.1. Magnetotelluric Inversion Methodology

Magnetotelluric data are collected by measuring the orthogonal, horizontal electric (E), and magnetic (H) field components in the time domain. After taking the Fourier transform, these components can be related using a 2×2 matrix of electrical impedances in the frequency domain (Chave & Jones, 2012):

$$\begin{bmatrix} E_x \\ E_y \end{bmatrix} = \begin{bmatrix} Z_{xx} & Z_{xy} \\ Z_{yx} & Z_{yy} \end{bmatrix} \begin{bmatrix} H_x \\ H_y \end{bmatrix},$$

(1)

where the subscripts x and y denote fields in the north and east directions, respectively, and all variables are functions of angular frequency, ω.

The MT inverse problem uses the frequency-domain electrical impedance data, $Z_{ij}(\omega)$, as a constraint to solve for a resistivity model of the Earth's subsurface. In most realistic MT surveys, the number of cells in the resistivity model is much larger than the number of data points to be used as a constraint and no unique solution exists. Thus, the inverse problem is ill-posed and requires an additional constraint or regularization (Parker, 1994). The underlying philosophy used in many approaches to MT inversion is that the resistivity
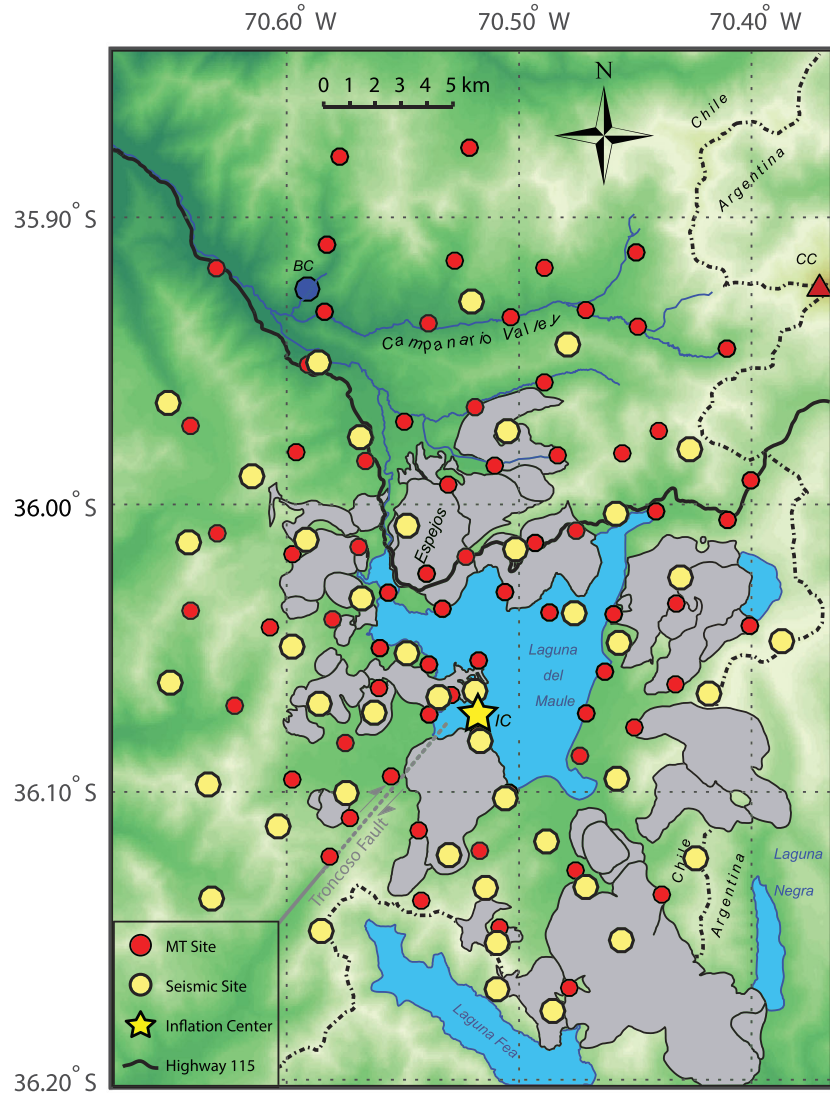
Figure 1. Map of Laguna del Maule Volcanic Field. Gray polygons are mapped lava flows from Andersen et al. (2017). Magnetotelluric site locations are red dots from Cordell et al. (2018). Seismic sites are yellow dots from Wespestad et al. (2019). BC = Baños Campanario hot springs; CC = Cerro Campanario; IC = inflation center.

model should be smooth with minimum structure (e.g., Constable et al., 1987; Egbert & Kelbert, 2012) and thus we seek to minimize the following objective function:

$$U(\mathbf{d}, \mathbf{m}, \lambda) = (\mathbf{d} - F[\mathbf{m}])^T \mathbf{C_d}^{-1}(\mathbf{d} - F[\mathbf{m}]) + \lambda(\mathbf{m} - \mathbf{m_0})^T \mathbf{C_m}^{-1}(\mathbf{m} - \mathbf{m_0}),\qquad(2)$$

where $\mathbf{d}$ is a $N \times 1$ vector containing real and imaginary MT impedance data for all sites, frequencies, and tensor components; $\mathbf{m}$ is the 3-D resistivity model rearranged into an $M \times 1$ column vector; $\mathbf{m_0}$ is a reference conductivity model (usually a halfspace) of the same size as $\mathbf{m}$; and $F[\mathbf{m}]$ is the forward operator which computes predicted impedance data (i.e., the predicted response) from $\mathbf{m}$. The data covariance matrix, $\mathbf{C_d}$, is an $N \times N$ matrix containing data errors (or weights) for each data point, $\mathbf{\Delta d}$, along the diagonal. The impedance data errors are often scaled with a relative error floor, $\varepsilon > 0$, as some fraction of the off-diagonal impedance magnitudes because statistical data errors calculated during time series processing are too small and do not capture frequency-to-frequency noise (see Miensopust, 2017). The model covariance matrix, $\mathbf{C_m}$, is an $M \times M$ matrix which is applied using spatial smoothing parameters, $0 < \gamma < 1$. The smoothing parameters are user-defined scalar values which can be made very versatile when constructing the model covariance matrix with different levels of smoothing in different orthogonal directions

(Kelbert et al., 2014; Robertson et al., 2020). The regularization (or trade-off) parameter, λ, weights the relative importance of each term in Equation 2.

The first term of Equation 2 is the data misfit penalty while the second term is the model norm scaled by λ. The data misfit penalty value is often reported as a scaled χ^2 statistic such as r.m.s. misfit:

$$r.m.s. = \sqrt{\frac{1}{N}(\mathbf{d} - F[\mathbf{m}])^T \mathbf{C_d^{-1}}(\mathbf{d} - F[\mathbf{m}])} = \sqrt{\frac{1}{N}\sum_{n=1}^{N}\left(\frac{d_n - F_n(m)}{\Delta d_n}\right)^2} = \sqrt{\frac{1}{N}\sum_{n=1}^{N}r_n^2}, \qquad (3)$$

where $\mathbf{r} = [r_1, r_2, ...r_N]$ is the vector of impedance data residuals normalized by the error.

Most algorithms used to minimize $U(\mathbf{d}, \mathbf{m}, \lambda)$ work by linearizing the objective function and then iteratively stepping toward the solution via $\mathbf{m}_{k+1}$ given some starting model $\mathbf{m_s}$ (e.g., Kelbert et al., 2014). The final model, $\mathbf{m_f}$, is one which minimizes the objective function. Note that the starting model ($\mathbf{m_s}$) and the reference model ($\mathbf{m_0}$ in Equation 2) are different. The reference model is used to impose spatial smoothing such that the final model, $\mathbf{m_f}$, is spatially smooth relative to $\mathbf{m_0}$. If the reference model is rough at a particular location (e.g., a sharp boundary at the ocean-Earth interface), then the final model will also be rough at that location. In contrast, the starting model simply tells the inversion from where to begin the minimization process and does not affect the spatial smoothing (Miensopust, 2017).

2.2. Statistical Analysis of Residuals From Inverse Model Perturbations

Hypothesis testing is carried out by taking a resistivity model and perturbing or manipulating it in some way by adding, removing, or replacing certain features of the model with a new resistivity value to explore the inverse solution space (Bedrosian, 2007). The most common method of hypothesis testing involves perturbing the preferred inversion model, $\mathbf{m_f}$, to create a new perturbed model, $\mathbf{m_p}$, and then computing the MT forward response (i.e., the perturbed response, $F[\mathbf{m_p}]$) and comparing it to the original inversion response (e.g., Baba et al., 2006; Becken et al., 2008; Burd et al., 2014; Thiel & Heinson, 2010). This method is relatively fast and only requires one forward computation of the perturbed model. In assessing whether the perturbed response is different from the original response, most MT practitioners have used either visual examination of the MT apparent resistivity and phase curves and/or the relative change in data misfit. Visually assessing the difference in the curves is subjective and the relative change in data misfit says nothing of whether the change is statistically significant or not. There is no agreed upon definition of how small the difference between two r.m.s. values must be before they are considered to be equivalent and different authors will have different ideas about how similar two r.m.s. values are. A notable example of being more quantitative is Baba et al. (2006) who used a two-sided F test to examine whether two distributions of residuals (e.g., the residuals from an isotropic model response and the residuals from an anisotropic model response) were statistically different within some confidence level. They used the ratio of the variances of the residuals (i.e., the ratio of the squared r.m.s. misfit values) as their test statistic. Their method was more statistically rigorous than simply comparing the relative difference in misfit and they were able to determine if a result was statistically significant.

There are two notable drawbacks to using the F test when perturbing models. The first is that it assumes both distributions of residuals (i.e., the original residuals and the perturbed residuals) are Gaussian. In the case of perturbing models, it is easy to envision scenarios where the perturbed model causes the perturbed residuals to no longer be Gaussian by introducing non-Gaussian outliers or skewed distributions. The second problem with the F test is that it only measures differences in the variance of the distribution while neglecting other aspects (e.g., the mean, modality, skewness). Thus, two sets of residuals with identical variance may have different means which go undetected by the F test.

In an effort to improve upon the assessment of the data fit of a perturbed model, additional statistical tests can be used to determine whether the sets of normalized residuals from the original inversion model ($\mathbf{r_{orig}}$) and the normalized residuals from a perturbed model ($\mathbf{r_{pert}}$) are drawn from the same underlying distribution. One of the most basic variants of this test is the two-sample Kolmogorov-Smirnov (KS) test which has been applied to MT data by Lee et al. (2020) with theory reviewed by R. L. Miller and Kahn (1962) and Massey (1951). The KS test is different from the F test in that (1) it simultaneously tests differences in mean, median, and variance; (2) it is nonparametric and makes no assumptions about whether the sets of residuals

are Gaussian; and (3) it is sensitive to upward and downward biasing whereas other variance-based measures (like the F test) measure only absolute distance. The test computes the maximum difference between the empirical cumulative distribution functions of each set of residuals. This maximum difference is called the D-statistic and can be compared to a critical value

$$D_{crit} = \sqrt{-\frac{1}{2}\ln(\alpha)}\sqrt{\frac{a+b}{ab}}, \tag{4}$$

where α is a user-defined significance level and a and b are the number of data points in each of the two sets of residuals. The D-statistic can be converted to a standard asymptotic p value which describes the probability of obtaining the results from the hypothesis test assuming that the null hypothesis is correct. The null hypothesis of the KS test is that the two sets are drawn from the same underlying distribution. This hypothesis is rejected if the KS test results in a p value less than α. It has been a common standard to use a significance level of $\alpha = 0.05$ such that a p value less than 0.05 is considered a "statistically significant" result (Fisher, 1925). If the KS test between two sets of residuals results in $p < 0.05$, then the result is considered statistically significant and the perturbation to the model is considered to be detected by the MT data because there is only a 5% chance that the null hypothesis is true. In other words, the change in the residuals can only be explained by random chance 5% of the time, but 95% of the time, the change is due to the perturbation. The KS test can be performed on any two sets of residuals and is very quick to compute. The KS test can also be used to compare individual sites or individual frequencies but throughout this paper the KS test is applied to the full set of residuals. This was done because the inversion algorithm minimizes the full set of residuals and does not discriminate between different subsets of the data.

A useful way to visualize the differences in two distributions of normalized residuals is to make a cross-plot of the two with the original residuals on the horizontal axis and the perturbed residuals on the vertical axis. The predicted data which are unchanged before and after a perturbation will plot along the diagonal line with slope of 1. Residuals which became smaller after the perturbation was added (i.e., predicted data became closer to the observed data point and have better fit with the perturbation) plot in the left and right quadrants bounded by diagonal lines with slopes of ± 1. Residuals which became larger after the perturbation was added (i.e., data fit was worse with the perturbation added) plot in the top and bottom quadrants bounded by the same diagonals. Cross-plots of residuals are not directly linked to the KS test but provide a useful visual queue to interpreting the KS test results.

2.3. A Priori Inversions and Fixed Inversions

When using 3-D inversions, the above method of hypothesis testing is desirable because it is relatively quick requiring only a single forward computation of the perturbed model. However, it is limited by the fact that it makes an implicit assumption that the original inversion model is the best-fitting model for the solution space and all perturbations are evaluated with this inversion model as a benchmark. It may be possible for the data to be equally well fit, or better fit, if the inversion algorithm is allowed to converge to a new minimum when the perturbation is included as an additional constraint on the solution. The constraint can be added in different ways and here we consider two of them.

An additional inversion test can be run which adds the perturbation to the starting model, $\mathbf{m_s}$, as *a priori* information and then the inversion is run and allowed to converge to a new solution. This is called an *a priori* inversion and it tests whether the additional information at the start affects the final solution. If the added perturbation is removed by the inversion algorithm, this strongly suggests that the data are sensitive to it and the data are better fit without it. A variation of this method can be run in which the model cells of the added anomaly are fixed throughout the inversion (i.e., fixed inversion). Fixing the anomaly model cells in the starting model explicitly tests whether the hypothesized feature can be fit to the data if the inversion is only allowed to alter the surrounding cells. It is worth noting that the fixed inversion changes the model covariance matrix and reference model ($\mathbf{m_0}$), while the *a priori* inversion does not. Thus, the *a priori* inversion has the same objective function but simply starts the inversion algorithm from a different location in the solution space while the fixed inversion changes both the objective function and the starting location.

Using either the *a priori* inversion method or the fixed inversion method may result in an inversion solution which has a similar or lower r.m.s. misfit to the original inversion which would imply that the data can be
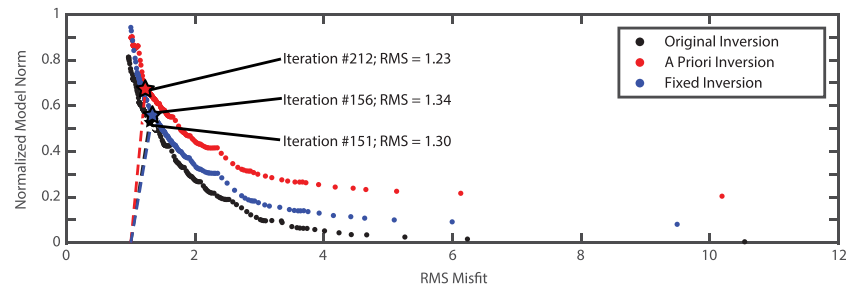
Figure 2. Model norm versus r.m.s. misfit convergence curves for the original (preferred) MT inversion (model shown in Figure 4) and the a priori inversion and the fixed inversion (both models shown in Figure 8). The dashed lines point to the preferred iteration nearest to an r.m.s. of unity and a model norm of zero. The stars denote the preferred iteration from each inversion.

adequately fit with or without the perturbation. However, the model may be significantly rougher (i.e., a larger model norm) and may include new artifacts and/or complicated structures that are geologically unrealistic. As mentioned earlier, the underlying philosophy of MT inversion is that resistivity models should contain minimum structure. It is preferable to examine both model norm and data misfit to see which inversion best balances the two terms in Equation 2. It is also possible to compare different inversion methodologies using the KS test and examine their residual distributions. Rather than simply comparing the r.m.s. misfit between two inversions, the KS test can be used to examine whether the two inversions have the same distribution of residuals. If they do, then there is a stronger case to be made that these two models are equally valid and can be interpreted as such. If the distribution of residuals is different, then it is more likely that the model responses are distinct within the uncertainty of the data.

3. Laguna del Maule Magnetotelluric Inversion Resistivity Model

As described above, much of the hypothesis testing workflow uses an existing "preferred" inversion model as a benchmark to compare with other perturbed models. As such, it is important to thoroughly examine the solution space before deciding on a preferred inversion model to interpret. When performing 3-D inversions, it is important to consider the inputs and how they will influence the output. In general, there are too many input variables to fully investigate the solution space including data selection, mesh design, inversion parameters, and inversion algorithm (Miensopust, 2017; Robertson et al., 2020). For this reason, any investigation of the inverse models must necessarily make certain choices as to which variables will remain constant throughout the investigation. All inverse modeling in this study used the ModEM inversion algorithm (Kelbert et al., 2014). A relative error floor of $\epsilon = 0.06$ was assigned to all four impedance elements as a fraction of $\sqrt{|Z_{xy}||Z_{yx}|}$. The inversion began with an r.m.s. misfit of 17.15 and converged to an r.m.s. of 1.00 after 291 iterations (Figure 2). The model covariance smoothing parameter was set to $\gamma = 0.3$, and a 100 Ωm halfspace model was used for $\mathbf{m_0}$ and $\mathbf{m_s}$. When defining the regularization parameter, ModEM has an automated scheme to decrease the regularization as the inversion algorithm proceeds in order to achieve good data fit. Because of this, the final model often gives little weight to the model smoothness and seeks only to minimize the data fit and thus results in rough models which may contain unrealistic resistivity values. To avoid this, a simple modified L-curve approach was used to define the iteration with the optimal regularization parameter which best balanced the trade-off between misfit and model smoothness. The iteration which was nearest to an r.m.s. of unity and a model norm of zero was considered the optimal model (Figure 2). Iteration 151 satisfies this condition and has an r.m.s. misfit of 1.30 and a model norm of 0.53. The supporting information shows an examination of the solution space by varying data error floor, model covariance smoothing parameter, and starting model halfspace value.

The data misfit between the observed MT data and the preferred inversion response is shown in Figure 3 in map view for each station and as a function of period and impedance component. In general, the r.m.s. misfit is relatively uniform both spatially and as a function of period with only some small outliers at long periods (>100 s). The misfit is similar for both diagonal and off-diagonal components and stations with higher misfit tending to be located on the edges of the array. The resistivity model is shown in Figure 4 using horizontal and diagonal slices. In general, the primary conductive features in this model are similar to those presented
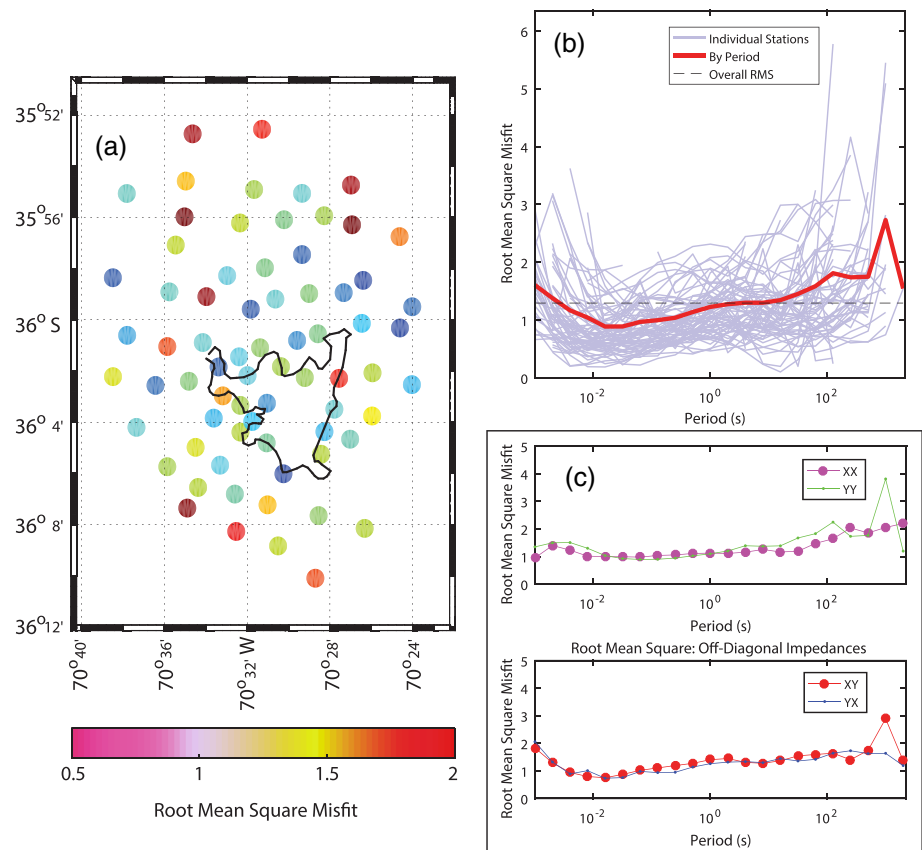
Figure 3. Data r.m.s. misfit for the preferred inversion model shown in Figure 4. (a) The r.m.s. misfit as a function of MT station; (b) r.m.s. misfit as a function of period for each station (blue lines) and all stations (red line); (c) r.m.s. misfit as a function of period for each component of the impedance tensor. Overall r.m.s. misfit is 1.30.

by Cordell et al. (2018). The model of Cordell et al. (2018) was not used directly because the data were reedited with a stricter criterion for removing outliers. The data set from Cordell et al. (2018) contained $N = 10,064$ data points and resulted in a model with an r.m.s. misfit of 1.47. The updated data set removed additional data points and resulted in a total of $N = 9,776$ data points with an r.m.s. misfit of 1.30. The overall differences between the model of Cordell et al. (2018) and the current model are negligible.

The resulting model shown in Figure 4 includes the upper crustal Espejos conductor (C3) with a very low bulk resistivity (minimum resistivity of 0.3 Ωm) at a depth of 3 km beneath the western side of the lake and the Espejos lava flow. This conductor dips to the north-northwest and was interpreted by Cordell et al. (2018) as a region of partial melt with a significant hydrothermal fluid component. Another primary conductive feature in the midcrust is the Campanario conductor (C4) at a depth of 9–10 km located to the north of the lake. The Campanario conductor was interpreted as a zone of partial melt with a melt fraction less than 35% (Cordell et al., 2018). It is important to note that the Espejos conductor (C3) is a conductive lobe connected to the Campanario conductor (C4) coming up toward the western side of the lake near the area of inflation center (labeled IC in Figure 4). There is also a weak conductor (labeled S1) on the southwest side of the lake which trends along the Troncoso fault, but it is not interpretable because it is not very conductive (e.g., >10 Ωm).

4. Incorporating Seismic Constraints Into the Magnetotelluric Modeling

4.1. Initial Comparison Between Preferred Resistivity Model and Seismic Velocity Model

A shear wave velocity (Vs) model of the LdMVF magmatic plumbing system was produced using surface wave tomography in a previously published study by Wespestad et al. (2019). Seismic data used in the inversion were collected with a temporary array of 43 seismic instruments with a 3–5 km station spacing and
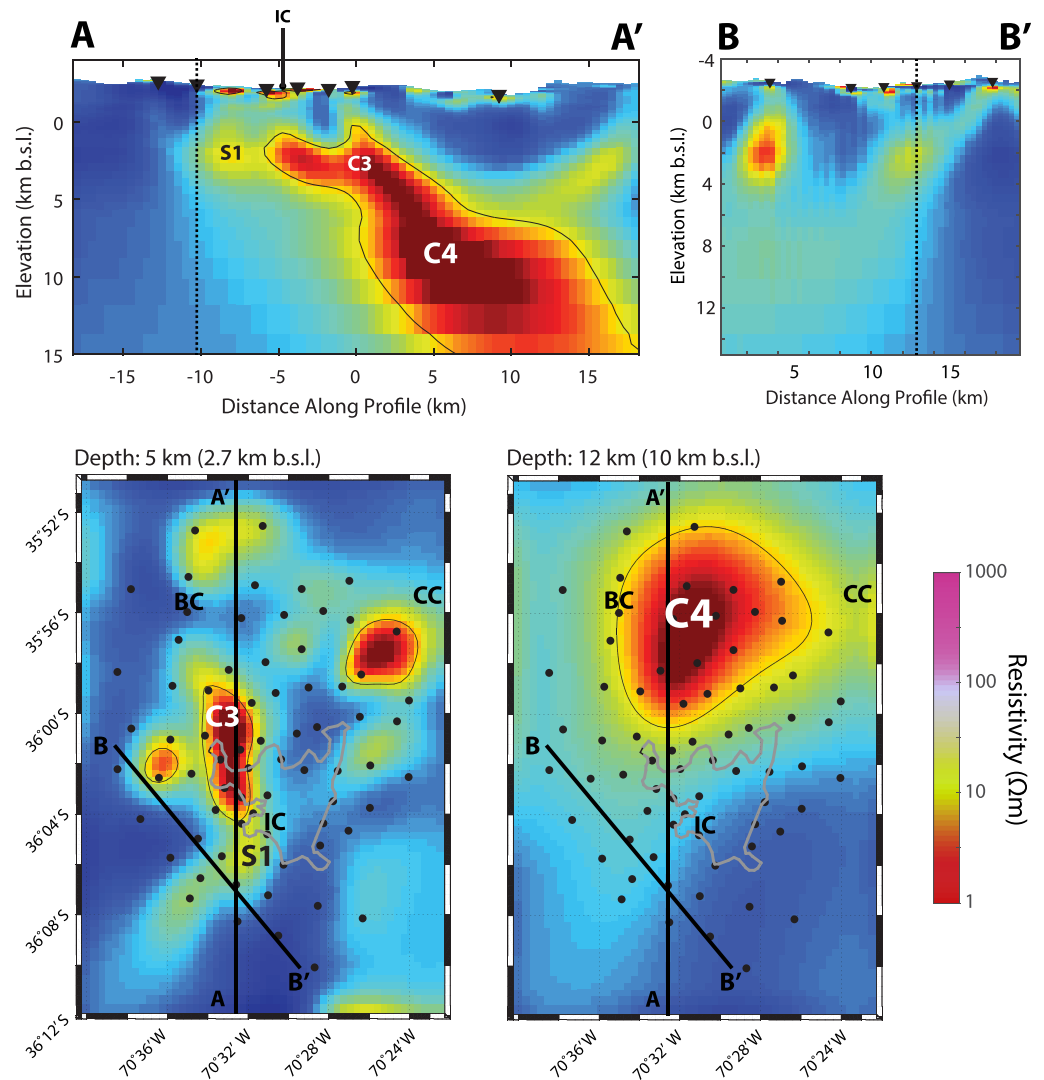
Figure 4. Preferred MT resistivity model shown using a north-south vertical slice along A-A', diagonal slice along B-B', and two horizontal slices at 5 (2.7 km b.s.l.) and 12 km (10 km b.s.l.) depth. Major interpreted features are labeled C3, C4, and S1 with thin black line showing the 10 Ωm contour. Black dashed lines on vertical sections show intersection of the profiles. Black dots on horizontal slices and inverted triangles on vertical slice are MT site locations. The outline of Laguna del Maule is shown in gray. IC = inflation center; BC = Baños Campanario hot springs; CC = Cerro Campanario stratovolcano.

centered on the LdMVF. The array covered a similar footprint to the MT array (Figure 1). Additional seismic data were collected at eight remote stations within approximately 75 km of the seismic array and incorporated into the seismic study (Wespestad et al., 2019). Wespestad et al. (2019) incorporated both ambient noise and earthquake coda correlations in order to increase the spatial resolution of their Vs model. One-dimensional inversions were performed at nodes spaced on a regular 3 km grid. These one-dimensional inversions where then interpolated onto a 3-D mesh which had horizontal and vertical cells with width of 750 and 250 m, respectively. The vertical cells also included two padding cells with thicknesses of 800 and 1,300 m such that the maximum depth of the model was approximately 9.5 km below sea level. The seismic model did not include topography but the top of the model was set to 2.45 km above sea level. The 3-D Vs model is shown in Figure 5 and includes one primary low-velocity zone (LVZ) on the western side of the lake between 2 and 8 km depth. This feature has a south-west strike and dips to the west-northwest. It is laterally offset from the center of observed deformation by several kilometers. The LVZ was interpreted as a 450 km^3 magma reservoir with an average melt fraction 5–6%. This surface wave-derived Vs model is amenable to comparison with the MT-derived resistivity
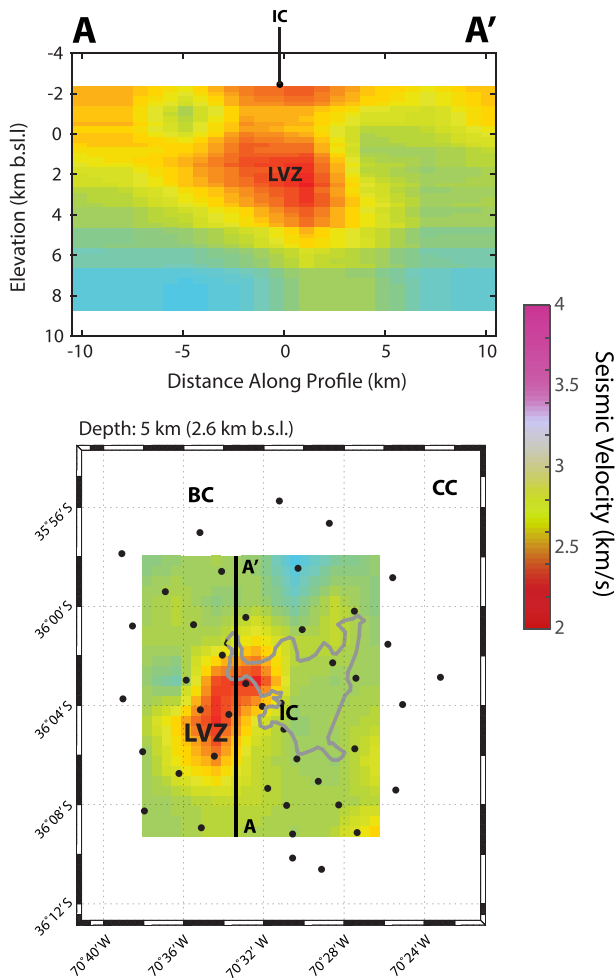
Figure 5. The surface wave shear wave velocity model from Wespestad et al. (2019) shown using a north-south slice along A-A' and a horizontal slice at 5 km depth (2.6 km b.s.l.). The model has no topography but has a model top defined at 2.45 km a.s.l. The interpreted low-velocity zone is labeled LVZ. Black dots on horizontal slice are seismometer locations and the outline of Laguna del Maule is in gray. IC = inflation center; BC = Baños Campanario hot springs; CC = Cerro Campanario stratovolcano.

model because of similarities in frequency-domain dispersive waves which are used as energy sources; seismic surface wave data use a dispersive elastic wave field whereas the MT method uses a dispersive electromagnetic wave field. A teleseismic tomography model of the LdMVF from Bai et al. (2020) shows a similar upper crustal LVZ as the Vs model from Wespestad et al. (2019). However, the parameterization of the teleseismic tomography model space is significantly coarser in the vertical direction (e.g., 4 km vertical cells) than the MT- and surface wave-derived resistivity and Vs model spaces making direct comparison to these models impractical.

There are some similarities between the resistivity model and Vs model but also some significant differences (Figures 4 and 5). The LVZ and C3 overlap on the western side of the lake but C3 dips to the north and is aligned north-south, while the LVZ dips to the west-north-west and trends southwest-northeast. The LVZ also extends further to the southwest and parallels the inferred location of the Troncoso fault (Figure 1; Garibaldi et al., 2020). This region has a moderately low resistivity of 10 Ωm (S1 in Figure 4) but still over an order of magnitude more resistive than C3. The inferred volume of the LVZ is also significantly larger than C3 and the melt fraction is interpreted to be very low (e.g., 5%) compared to the inferred melt fraction of C3 (e.g., >35% plus hydrothermal fluids). The fact that the Vs model does not image the deeper feature to the north (C4) is likely due to the sparse seismic station coverage in this region. As a result, the primary features of interest in comparing the Vs and resistivity models are the LVZ and C3. These features are located in regions of their respective model spaces where data coverage provides acceptable spatial resolution. Thus, the following analyses examine whether the differences between C3 and the LVZ are due to the resolution and nonuniqueness of their respective geophysical methods or if these differences are due to the geology, geometry, and/or composition of the magma-hydrothermal system.

Bouguer gravity data and time-lapse gravity data have also been collected at the LdMVF by C. A. Miller, Williams-Jones, et al. (2017) and C. A. Miller, Le Mével, et al. (2017), respectively. These are discussed in relation to the MT data in detail by Cordell et al. (2018). The primary conclusion was that the low-density feature interpreted from the Bouguer data (C. A. Miller, Willliams-Jones, et al., 2017) was likely too small and/or had too low a melt fraction to be imaged by the MT data. The MT data placed important constraints on the available interpretations of the gravity data (Cordell et al., 2018).

4.2. Statistical Analysis of Residuals From Model Perturbations

To examine the MT data sensitivity to the LVZ, the Vs model was first interpolated onto the resistivity model mesh. The volume of the LVZ was defined by finding model cells in each layer which were more than one standard deviation below the mean velocity of that layer. The top 3.5 km of the Vs model was excluded (i.e., all model space shallower than 1 km b.s.l.) because the Vs model did not include topography and the seismic data do not have high enough frequencies to reliably image the near-surface structure. The total volume of the LVZ calculated with this method was 442 km^3, similar to the volume of 450 km^3 estimated by Wespestad et al. (2019) which used the velocity reversal at nodes to define the LVZ. In the resistivity model, the model cells occupying the volume of the LVZ were varied over 12 different resistivity intervals between 1 and 100 Ωm. These are a set of perturbed models representing the LVZ as a homogeneous magma reservoir with the 1 Ωm case shown in Figure 6. The bulk resistivity of the anomaly is a function of the melt fraction, chemical composition, water content, temperature, and pressure with the melt fraction being the primary factor (Glover et al., 2000; Guo et al., 2016). Each bulk resistivity value
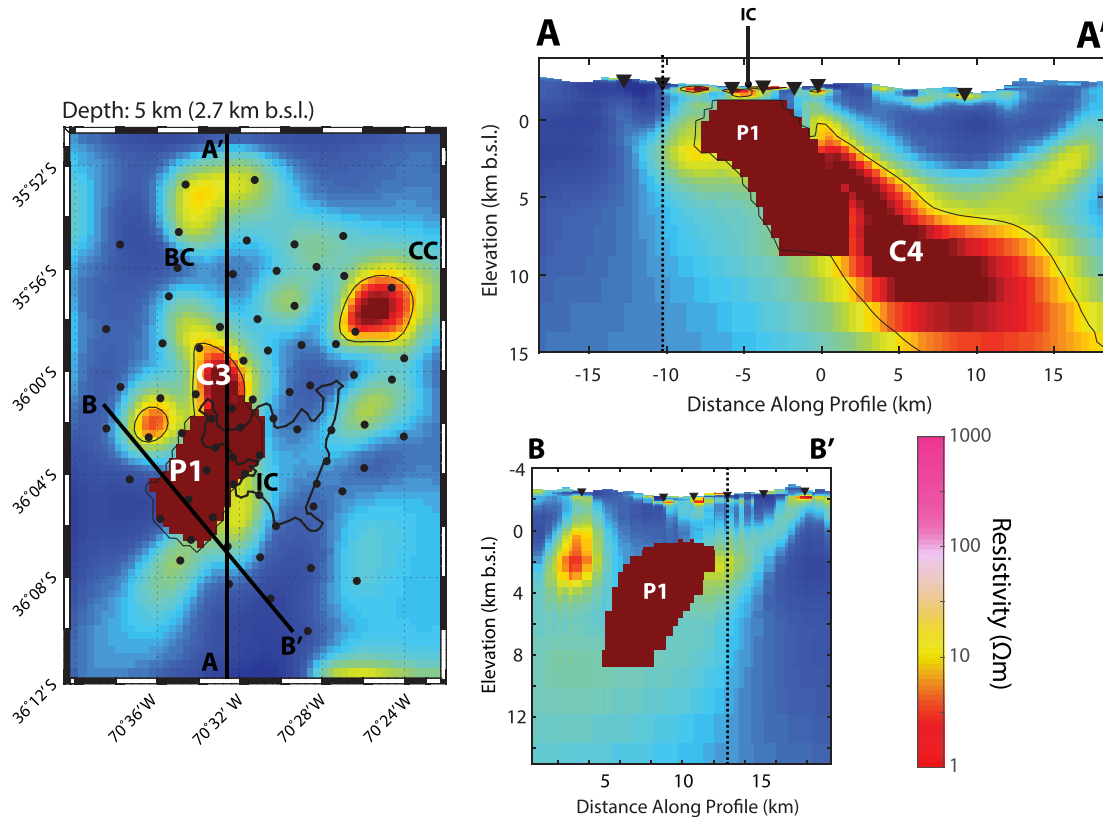
Figure 6. The preferred MT resistivity model with perturbation (P1) added. The model is shown with a horizontal slice at 5 km (2.6 km b.s.l.) and two vertical slices along profiles A-A′ and B-B′. The shape and location of P1 is determined by the shape of the 450 km³ low seismic velocity anomaly as defined in text. In this figure, the model cells encompassed by P1 have a value of 1 Ωm. Black dashed lines on vertical sections show intersection of the profiles. Black dots on horizontal slice and inverted triangles on vertical slices show locations of MT sites. IC = inflation center; BC = Baños Campanario hot springs; CC = Cerro Campanario stratovolcano.

represents an approximate melt fraction for a shallow rhyolite melt at 800°C, 5 wt% water content, and 150 MPa. Such a melt has an estimated melt resistivity of 0.4 Ωm and the bulk resistivity is calculated using Modified Archie's law (Cordell et al., 2018; Glover et al., 2000; Guo et al., 2016). A low-temperature, relatively homogeneous crystal mush with melt fraction less than 10% is a realistic scenario for the magma storage conditions at silicic systems because a smaller temperature contrast and a lack of convection decreases the cooling rate which can allow for more long-lived reservoirs (Bachmann & Huber, 2016). However, a homogeneous, higher melt fraction reservoir (>10%) would be less realistic and represent either the largely discredited "big tank" conceptual model (e.g., Annen et al., 2015) or a system in the late-stage of a significant, transient rejuvenation episode immediately preceding an eruption (Szymanowski et al., 2017). For completeness, a variety of different melt fractions (from approximately 2% to 50%) were investigated even if some were more geologically implausible than others. The MT data were calculated for each perturbed model to obtain the perturbed model response.

The normalized residuals of the original inversion response were then compared to the normalized residuals of the perturbed response using the KS test, F test, and cross-plots. A summary of these perturbed models and statistical tests is shown in Table 1. As can be seen in Table 1, all the models resulted in a statistically significant ($\alpha = 0.05$) difference in the distributions of residuals using the KS test. This implies that the distribution of residuals from the perturbed model responses is different from the distribution of residuals from the original inversion response with a high degree of confidence. This further suggests that the size and location of the LVZ is incongruous with the preferred resistivity model, assuming that the LVZ represents a homogeneous magma reservoir with some spatially uniform melt fraction. Table 1 also shows the difference in r.m.s. misfit and the ratio of the squared r.m.s. misfits (i.e., the ratio of the variance; Baba et al., 2006). Recall that the original inversion had a misfit of 1.30. As can be seen, the difference in r.m.s. misfit is

Table 1
Statistical Analysis of Responses From the Resistivity Model Which Includes the Volume of the LVZ as a Perturbation (P1) With Various Bulk Resistivity Values

Bulk resistivity of perturbation (Ωm)	Approximate melt fraction (%)	Overall KS test p value ($\alpha = 0.05$)	Difference in r.m.s. misfit	Ratio of squared r.m.s. misfit
1	50	1×10^{-24}	1.38	4.25
3	25	2×10^{-15}	0.90	2.86
10	10	3×10^{-4}	0.26	1.44
15	8	0.017	0.13	1.21
20	7	0.0096	0.09	1.14
25	6	0.0060	0.09	1.14
30	5.5	0.0069	0.11	1.18
35	5	0.004	0.15	1.24
40	4.5	0.0046	0.18	1.30
50	4	0.0014	0.25	1.42
80	3	5×10^{-5}	0.41	1.73
100	2	1×10^{-5}	0.48	1.87

Note. Approximate melt fractions are estimated using Modified Archie's law (Glover et al., 2000) with a 0.4 Ωm melt resistivity. The melt resistivity is calculated using the empirical relation of Guo et al. (2016) for an 800°C water-saturated melt with 5 wt% water content at 150 MPa. Using the KS test, a p value $< \alpha$ signifies a statistically significant difference between the distributions of residuals suggesting that the LVZ-defined resistivity anomaly has been detected. Using the F test, a ratio of squared r.m.s. misfit values greater than 1.034 also suggests statistically significant differences in misfit ($\alpha = 0.05$).

quite small for many of the models which may lead to the conclusion that the perturbed model response is statistically the same as the original model response. However, according to the F test with 9,776 degrees of freedom and a significance level of $\alpha = 0.05$, if the ratio of the squared r.m.s. misfit values lies outside the bounds (0.9673,1.034) then the null hypothesis should be rejected. All the ratios in Table 1 lie outside those bounds, suggesting that all perturbations have a statistically significant impact on the r.m.s. misfit. In summary, despite a relatively small change in r.m.s. misfit, the distributions of residuals are statistically distinct, as indicated by both the KS test and the F test.

Figure 7 illustrates these differences visually by showing cross-plots of the residuals for the forward response with the 1, 3, 15, 50, and 100 Ωm anomalies added. The horizontal axis shows the normalized residuals from the original inversion while the vertical axis shows the normalized perturbed residuals. Blue points show residuals which became larger (i.e., farther from the true data point) after adding the anomaly while red points show residuals which became smaller (i.e., nearer to the true data point). The 1 and 3 Ωm responses have similar cross-plots with a large number of points with worse misfit after the perturbation was added and significantly more spread in the vertical direction versus the horizontal direction indicating more spread in residuals with the perturbation added. The 100 Ωm response has residuals which are biased to the lower half of the plot. This implies that impedances were, on average, becoming more positive after the perturbation was added (e.g., apparent resistivity is biased up). The 15 and 50 Ωm cross-plots also look similar although, in general, the 50 Ωm cross-plot has more scatter and a slightly lower p value.

4.3. A Priori Inversion

The above method uses the original MT inversion model as the basis for evaluating perturbations. However, it is possible that the data could be fit better or achieve a more reasonable model if given additional information to begin the inversion. In this case, the 15 Ωm anomaly (LVZ) was added to the 100 Ωm halfspace as a starting model ($\mathbf{m_s}$) as shown in the top row of Figure 8. The 15 Ωm anomaly was chosen because it had the smallest impact on the MT data when added to the original inversion model, even though it was still statistically significant ($p = 0.017$). Because the inversion is time-consuming and computationally intensive, it was not realistic to test the inversions with all of the different resistivity values from 1 through 100 Ωm. The reference model, $\mathbf{m_0}$, remained unchanged as a 100 Ωm halfspace and the covariance matrix remained unchanged. Running the inversion with the *a priori* starting model tests whether the starting model provides useful information which results in a model with better data fit. The *a priori* inversion allowed all model cells to change as the inversion progressed. The *a priori* inversion began with an r.m.s. misfit of 15.54 and converged to an r.m.s. misfit of unity after 299 iterations. Iteration 212 optimized both model norm and data
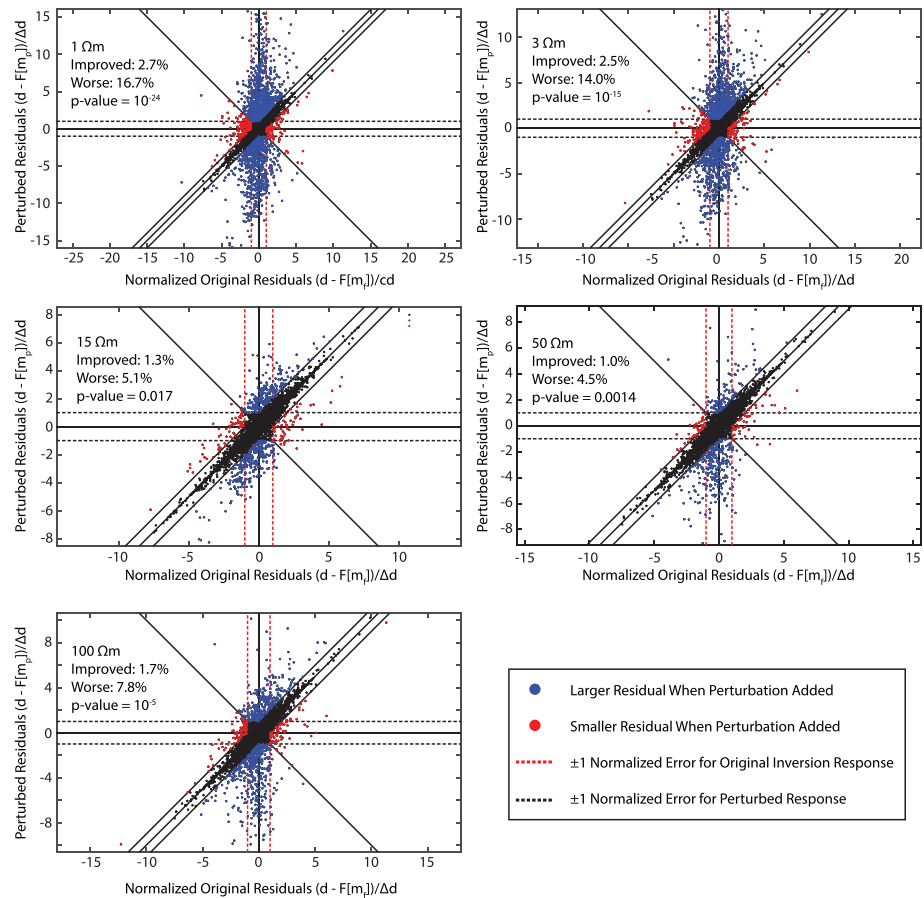
Figure 7. Cross-plots of normalized impedance residuals. The horizontal axis for each plot shows the normalized residuals from the original (preferred) MT inversion response. The vertical axis on each plot shows the normalized residuals from a perturbed MT response. Five perturbations are shown with P1 = 1, 3, 15, 50, and 100 Ωm.

misfit with an r.m.s. misfit of 1.23 and normalized model norm of 0.68 using a modified L-curve criteria to define the best model before the regularization parameter was reduced (Figure 2). The misfit is somewhat better than the original model misfit (r.m.s. misfit = 1.30) but the model norm is higher. As mentioned earlier, the KS test can be used to examine the differences between any two sets of residuals. Here the original inversion residuals and the *a priori* inversion residuals are compared using the KS test and result in a *p* value of 0.03. The combination of a statistically significant difference in residuals and lower r.m.s. misfit suggests that the *a priori* inversion results in a distinct model response within the uncertainty of the data with better data fit.

The optimal model from the *a priori* inversion is shown in the middle row of Figure 8 using the same horizontal, vertical, and diagonal slices as Figure 6. The Campanario conductor (C4) remains unchanged upon adding the LVZ to the starting model when compared to the original inversion (Figure 4). But the geometry of the Espejos conductor (C3) changes in some notable ways. The depth to C3 is somewhat greater (e.g., 4 km below surface) and the top of C3 is flatter which better agrees with the interpretation of the top of C3 as a sill around 4 km depth related to the ongoing inflation. This suggests that the geometry of the top of C3 is not well-constrained by the MT but the *a priori* information from the seismic provides an additional constraint. Furthermore, the base of C3 retained a sharper boundary along the bottom of the LVZ suggesting that the MT data are not very sensitive to the bottom of C3. The connection between C3 and C4 is also steeper which suggests that the dip of C3 is not well constrained in the original model and a steeper conductor is possible. It is more realistic to interpret a steeply dipping conductor as a conduit for partial melt from C4 to the inflation center rather than a shallow dipping conduit due to buoyancy forces although this interpretation depends on the strength of the overlying lithology relative to the fault weak zone.
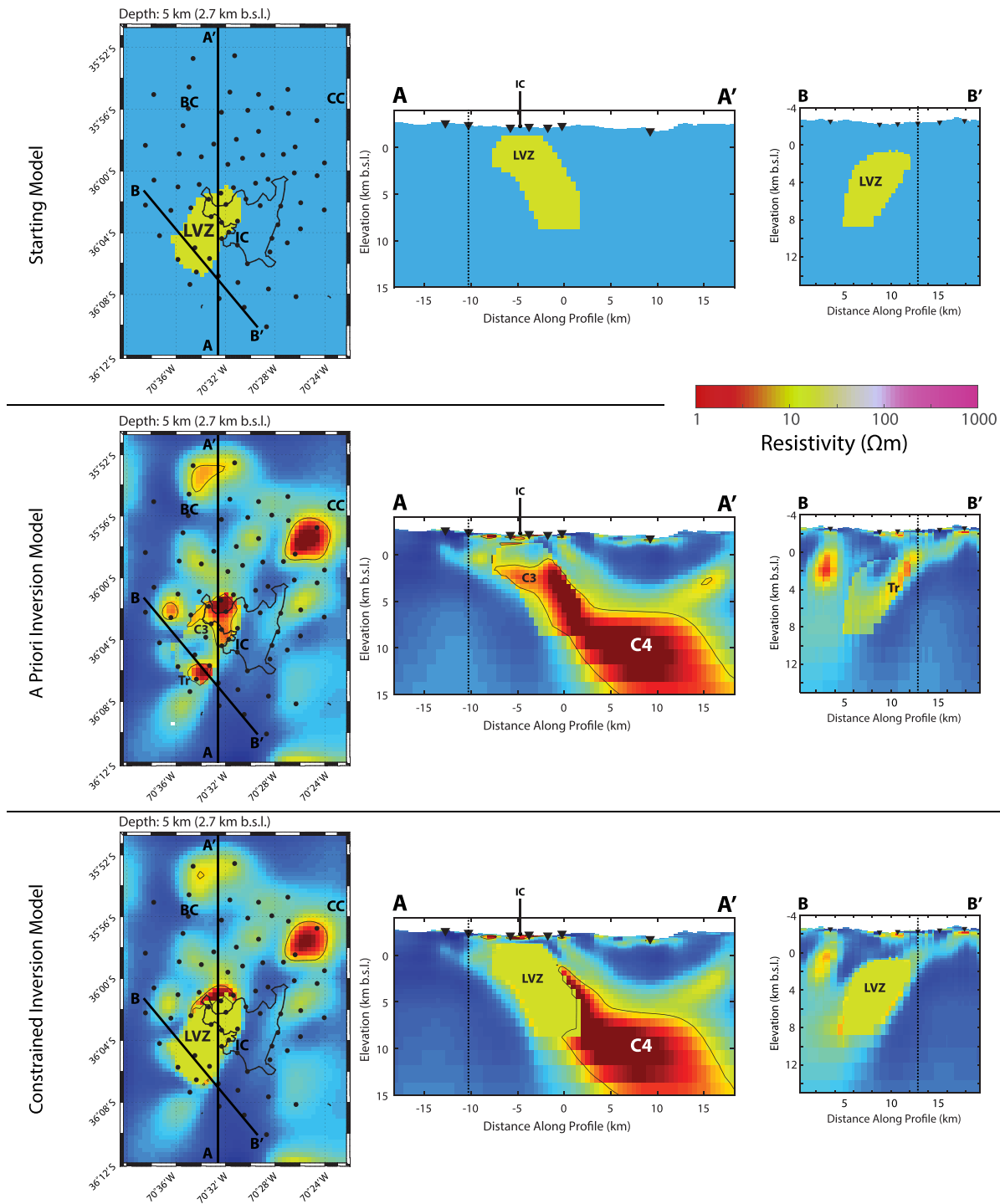
Figure 8. MT resistivity models from the a priori and fixed inversion cases. The top row shows the starting model used for both the a priori and fixed inversion. This model a 15 Ωm anomaly embedded in a 100 Ωm halfspace representing the low-velocity zone (LVZ). The second row shows the results from the a priori inversion using a 100 Ωm halfspace as the reference model. The third row shows the results from the fixed inversion in which the model cells in the LVZ are fixed. Slices are the same as Figure 6.

There is a more pronounced conductor to the southwest (Tr) near the Troncoso Fault which dips steeply to the northwest. This Troncoso conductor may be related to fluids or partial melt in the fault system and has a similar strike and dip to the Troncoso Fault (Garibaldi et al., 2020). It is also important to note that some parts of the LVZ become more resistive. The western part of the seismic velocity anomaly returns to
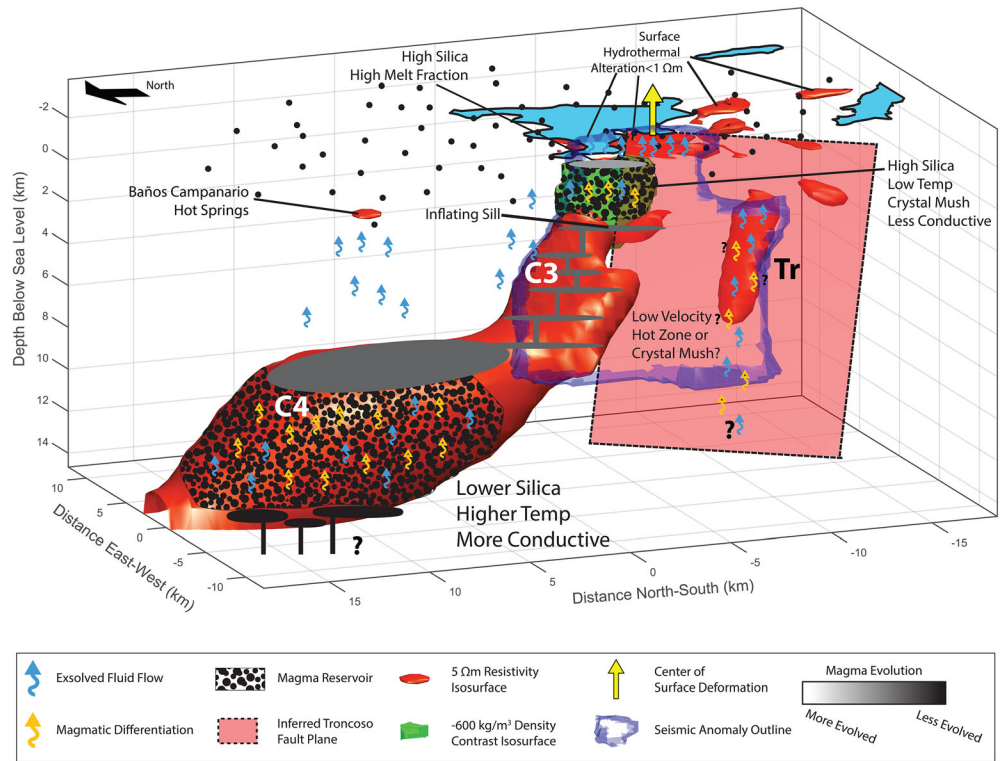
Figure 9. Three-dimensional conceptual model of the Laguna del Maule Volcanic Field looking southeast. The a priori inversion resistivity model is shown using a 5 Ωm isosurface. The density model of C. A. Miller, Williams-Jones, et al. (2017) is shown with a −600 kg/m³ isosurface. The seismic velocity model of Wespestad et al. (2019) is shown using the isosurface described in the text.

approximately the halfspace value (i.e., near 100 Ωm) and the shallowest portions of the seismic anomaly (e.g., <1 km b.s.l.) become similarly resistive. Like the model perturbations in section 4.2, this further suggests that the MT has a greater ability to resolve discrete features (e.g., a separation between C3 and Tr) whereas the seismic data tends to either blur these features together into a more homogeneous anomaly or is simply not able to resolve them.

4.4. Fixed Inversion

The second inversion modeling methodology is similar to the method described above. The difference is that the model shown in the top row of Figure 8 is used as both the reference model, $\mathbf{m_0}$, and the starting model, $\mathbf{m_s}$, with the model cells of the LVZ fixed at 15 Ωm for all iterations by changing the model covariance $\mathbf{C_m}$. This helps explicitly test whether a 15 Ωm melt reservoir can fit the MT data as well as the unconstrained original inversion with similar model norm. This fixed inversion began with an r.m.s. of 15.54 and converged to an r.m.s. misfit of approximately unity after 255 iterations and the optimal model was found at Iteration 156 with an r.m.s. misfit of 1.34 and normalized model norm of 0.56 (Figure 2). This resistivity model has higher data misfit and higher model norm than the original inversion, suggesting both poorer data fit and a greater deviation from the minimum-structure ideal of smooth MT inverse solutions. It is also worth noting that the model norm in this case is compared to a different reference model: the optimal model is spatially rough with sharp boundaries but the norm is still reasonable because it is in reference to a spatially rough reference model. Interestingly, the KS test between the two sets of residuals results in a *p* value of 0.54 which is above the threshold of significance. This suggests that the distributions of residuals are not distinct within the uncertainty of the data. This highlights inversion nonuniqueness and shows that the inversion can fit the data with neither better nor worse fit from the original inversion when the LVZ-defined anomaly is fixed, if it is allowed to change the model space outside the anomaly.

The resistivity model is shown in the lower row of Figure 8. Similar to the model from the *a priori* inversion (middle row of Figure 8), the model from the fixed inversion model has no noticeable change to the geometry

or location of the Campanario conductor (C4). The Espejos conductor (C3) is mostly subsumed by the fixed 15 Ωm LVZ anomaly. This suggests that the LVZ anomaly can be adequately fit by the MT data using a 15 Ωm resistivity value if the model is allowed to change around those fixed model cells and a rough model with sharp boundaries is allowed.

5. Discussion and Conclusions

This study aimed to evaluate the differences between the MT resistivity model and a previously published seismic velocity model to better understand the magma plumbing system beneath the LdMVF. This analysis resulted in three different inversion resistivity models of the subsurface: (1) the original inversion model, (2) the *a priori* inversion model, and (3) the fixed inversion model. It also included 12 additional perturbed models of the subsurface used for forward modeling hypothesis tests. This analysis highlights that the MT inversion models are nonunique, as expected, and a wide range of possible models exist, many of which result in reasonable data fits. However, based on this analysis, it can be shown that the MT data are best fit when the seismic anomaly is separated into discrete features (C3 and Tr) rather than combined into a homogeneous conductive (or resistive anomaly). This is borne out by three lines of evidence:

1. The KS test gave statistically significant results (p value < 0.05) when comparing the distribution of residuals for all perturbed models. No homogeneous perturbation was able to fit the MT data as well as the original inversion model. This suggests that the previously published seismic velocity and resistivity models are incongruous within the uncertainty of the MT data assuming both represent relatively homogeneous regions of melt.
2. The *a priori* inversion splits the low resistivity seismic anomaly into discrete conductors separated by a resistor and results in a model with a better data fit and a set of residuals which is statistically distinct from the original inversion. This suggests that the data are best fit with discrete conductors rather than a homogeneous anomaly.
3. The fixed inversion has the highest data misfit of all three inversions and, by necessity, contained sharp boundaries (and is thus a rougher model). A guiding philosophy in MT inversion is that minimum-structure, smooth solutions are preferable. If a rough model had much better data fit than a smooth solution, then it may be preferred, especially if it better aligns with other geological or geophysical results. However, in this case, the fixed inversion is neither smoother nor is it better fit by the data and is thus not the preferred solution.

Therefore, the *a priori* inversion model is the resistivity model which best incorporates the velocity model into the resistivity model and interpretation. The fact that the MT data are best fit by discrete conductors within the LVZ rather than a single anomaly suggests that differences in the methods are a real discrepancy indicating differences in magma storage conditions rather than solely an apparent discrepancy. The inclusion of the seismic velocity anomaly in the *a priori* model helps to better define the geometry of the Espejos conductor (C3) as a more steeply dipping feature which makes the interpretation of the conductor as a magmatic conduit (or dyke) from C4 to the surface more plausible given the steeply dipping Troncoso fault and observed transtensional normal faults (Garibaldi et al., 2020; Peterson et al., 2020). Furthermore, the *a priori* inversion model defines the Troncoso conductor (Tr) more clearly and may indicate the presence of fluids or partial melt in the fault system to the southwest. This geometry also agrees well with the location of significant crustal seismicity (Cardona et al., 2018). Finally, it is important to recognize that neither the *a priori* inversion nor the fixed inversion influenced the depth or geometry of the Campanario conductor (C4). It appears that this conductor is too far to the north and too deep to be strongly influenced by the shallow features near the inflation center.

A 3-D conceptual model of the LdMVF trans-crustal magmatic-hydrothermal system is shown in Figure 9 and is based on the *a priori* MT inversion model, and other published geophysical results. At a depth of 10 km in the midcrust, there is a zone of partial melt (C4) imaged by MT to the north of the LdMVF which was not detected by the current surface wave array. Less-evolved, crystal-poor melts originating deeper in the lower crust and mantle likely supply heat to maintain supersolidus temperatures. There may be some differentiation within this midcrustal magma reservoir, with crystal-poor silicic melts concentrated near the top.

A conduit from C4 to the inflation center is imaged as C3. This suggests that partial melts at the top of C4 are low viscosity (e.g., higher melt fraction) and they migrate both laterally (southward) and vertically (upward) along a preexisting structural boundary, i.e., the Troncoso fault. The top of C3 is flat at 4 km depth below surface and is at a similar depth as the inferred inflating sill from geodetic methods (Feigl et al., 2014; Le Mével et al., 2015). Petrological results from Klug et al. (2020) suggest that hydrated magma ascends from 14 to 4 km depth in good agreement with the interpretation of magma movement from C4 toward the surface via C3. Along with partial melt, there is also likely a significant hydrothermal component to the system with exsolved fluids derived from partial melts since petrological results suggest water-rich magmas at depth with up to 8 wt% H_2O and CO_2-rich mafic recharge which drives fluid exsolution (Klug et al., 2020). Some of these exsolved fluids may reach the surface at hot springs such as Baños Campanario, which has magmatic isotopic signatures (Benavente et al., 2016), and hydrothermal alteration at shallow depths beneath the LdMVF—both of which are imaged as shallow conductors in the MT model (Figure 9).

To the southwest, along the Troncoso fault is another conductor (Tr) likely related to fluids and partial melt and also linked to observed seismicity. The source of fluids in Tr is unclear. They could originate from a deeper feature directly below Tr or travel laterally from C3 along the Troncoso Fault. The presence of a large, low-velocity seismic anomaly which encompasses both C3 and Tr suggests that much of the subsurface between the two conductive features is at high temperature (but subsolidus) and/or is partially molten as a crystal mush with low melt fraction. Seismic methods are sensitive to bulk rock properties whereas MT determines resistivity that is sensitive to the presence of connected phases. Thus, the seismic data may be sensitive to a larger region of poorly connected mush that contains less than 5% melt and is relatively resistive (e.g., 100 Ωm). The MT data are primarily sensitive to regions of well-connected, higher melt fraction partial melt, and/or hydrothermal fluids within the shallow magmatic system. These smaller, discrete features may not be resolvable with the seismic array since Wespestad et al. (2019) used checkerboard tests to show that any feature smaller than approximately 6 km horizontally and 3 km vertically would likely go undetected. Further seismic resolution tests which explicitly include the geometry of C3 could confirm whether a magma reservoir with the geometry of C3 is resolvable. It is generally difficult to use geophysical methods to image the internal structure of a magma body since geophysical methods sample large volumes and thus anomalies are interpreted as having relatively homogeneous bulk properties (Lowenstern et al., 2017). However, despite these challenges, combining the MT and seismic results suggests that each method may be imaging important aspects of the same system; the seismic data image a large region of low melt fraction crystal mush while the MT data image smaller, more discrete features which are likely higher melt-fraction (or more fluid-rich) and thus represent the more mobile, eruptible components of the trans-crustal system.

A small, shallow, low-temperature region of partial melt directly beneath the observed inflation center has been imaged by Bouguer gravity (green in Figure 9; C. A. Miller, Williams-Jones, et al., 2017). This shallow magma reservoir is likely too small to be imaged by the MT or surface wave seismic data described in this paper. It is possible that the low-density Bouguer anomaly is partly due to gas-rich layers similar to that described at Mammoth Mountain (Sorey et al., 1998). Such a layer would make the low-density feature more resistive and thus more difficult to image with MT. At the top of the shallow magma reservoir is a lens of higher melt fraction and/or hydrothermal fluids which is imaged by time-lapse gravity measurements and MT (Cordell et al., 2018; C. A. Miller, Le Mével, et al., 2017).

The complex geometry and multiphase interpretation are in broad agreement with petrological studies at the LdMVF which also suggest a high degree of thermal complexity within the magma system and spatiotemporal variation in eruptive products (Andersen et al., 2019, 2018, 2017). Andersen et al. (2019) suggest the magma system may be thermally heterogeneous with coexisting hot and cold storage conditions. In this model, eruptible crystal-poor rhyolite melt (>85% melt) is relatively ephemeral within a longer-lived dacitic/andesitic rigid sponge with <15% melt (Andersen et al., 2019, 2018). The rigid sponge is heated from below via intermediate-to-mafic recharge. Erupted material does not appear to originate directly from the rigid sponge but rather from magma intrusion which produces regions of warmer, more mobile extractable mush (25–50% melt) from which crystal-poor melt can be extracted. In summary, the model of Andersen et al. (2019) includes three types of partial melt in a thermally heterogeneous system: crystal-poor eruptible melt (>85% melt), extractable mush (25–50% melt), and rigid sponge (<15% melt). The resistivity model suggests an ongoing intrusion event as magma moves from C4 in the midcrust (>10 km) toward the observed inflation

center closer to the surface (4 km), in agreement with magma ascent pathways from previous eruptions estimated using melt inclusions (Klug et al., 2020). This recharge event may have mobilized the larger rigid sponge to form localized regions of higher melt fraction extractable mush. This extractable mush is higher melt fraction than the rigid sponge and likely better connected and thus more conductive. The extractable mush is imaged in the MT resistivity model as C3 in the upper crust beneath the Espejos lava flow while the Vs model images the larger rigid sponge. Crystal-poor rhyolite melt is extracted from the extractable mush and migrates toward the region of ongoing deformation. The region of accumulation of crystal-poor eruptible rhyolite melt is relatively small, consistent with petrological evidence that eruptive batches are small and ephemeral (Andersen et al., 2018). The fact that the geophysical anomalies are both concentrated in the northern and northwestern LdMVF suggests that the ongoing deformation episode may be due to a resumption of significant magma intrusion from C4. Eruptions have largely been concentrated in the southeast LdMVF since the Late Pleistocene (14.5 ka) although the largest recent eruption occurred in the northwest (Rhyolite of Laguna del Maule, 19 ka), and even larger eruptions in the past also occurred in the northern LdMVF (e.g., the Bobadilla caldera, 950 ka) (Andersen et al., 2017; Hildreth et al., 2010). Resumption of eruptive activity in the northern LdMVF could also correspond to an increase in future volcanic hazards.

Most conceptual models show purely vertical ascent of intermediate-to-mafic recharge at silicic systems (e.g., Cashman et al., 2017; Zellmer & Annen, 2008). But a growing body of evidence suggests that laterally offset magma reservoirs may be common (Lerner et al., 2020). Alternative conceptual models (e.g., Cruden & Weinberg, 2018) show magma which migrates along the path of least resistance and, if there is a fault or litho-structural boundary in the crust, magma will preferentially travel along that boundary. The LdMVF may be a case where magma originates in a region that is laterally offset from the location of surface eruptions. The Troncoso fault is mapped as a major normal fault which dips to the northwest (Garibaldi et al., 2020). The dip of the fault may decrease with depth as a listric extensional fault which facilitates lateral transport of melt from C4 to the inflation center. There are other examples of lateral offset of magma and/or fluids at other volcanos at various spatial scales such as El Hierro, Canary Islands (Klügel et al., 2015), Yellowstone (Kelbert et al., 2012), Iceland (Bato et al., 2018), and Japan (Brothelande et al., 2018). Lerner et al. (2020) provide a database of such volcanoes from 2000 to 2018. Faulting is specifically linked to lateral magma supply at Osorno volcano in South Chile (Díaz et al., 2020). Numerical experiments have suggested that certain magma storage conditions and lithological or rheological discontinuities can facilitate lateral movement of melt and impact deformation source estimates (e.g., Masterlark et al., 2010; Pinel & Jaupart, 2004). Reflection seismic studies have also shown large lateral movement of magma in ancient magma plumbing systems (Magee et al., 2018). The results in this study as well as others highlight that it may often be necessary to design geophysical surveys which extend beyond the boundaries of the surface vents and lava flows to capture the full extent of magma plumbing systems.

The results here suggest that the LdMVF magmatic system is a structurally complex, multiphase system and presents an example of using multiple geophysical methods to probe different aspects of the magma plumbing system. In general, the analyses of this study show that differences between the MT and seismic methods are related to geological differences rather than the nonuniqueness of geophysical inversions and thus the discrepancies are interpreted as real discrepancies rather than apparent discrepancies. It is shown that MT can be used to image pathways of melt migration and identify regions of mobile melt with high melt fractions. Seismic tomography is sensitive to bulk properties of the subsurface which makes it amenable to identifying lower melt fraction mushes. Together, these methods provide a complementary picture of the LdMVF system. The seismic tomography results capture the full extent of the partially molten system, which would otherwise go undetected by MT. The MT data are able to detect smaller batches of magma within the thermally heterogeneous system. Further analysis of the resolution of the velocity model (e.g., by including the geometry of the conductive features for hypothesis testing and constrained inversion) as well as full joint inversion of the MT and surface wave data sets would further elucidate differences and similarities between the methods to better image the magma plumbing system at the LdMVF.

Data Availability Statement

Magnetotelluric data and resistivity models are available at the PANGAEA data repository (https://doi.pangaea.de/10.1594/PANGAEA.923790).

References

Afanasyev, A., Blundy, J. D., Melnik, O., & Sparks, S. (2018). Formation of magmatic brine lenses via focussed fluid-flow beneath volcanoes. *Earth and Planetary Science Letters*, *486*, 119–128. https://doi.org/10.1016/j.epsl.2018.01.013

Andersen, N. L., Singer, B. S., & Coble, M. A. (2019). Repeated rhyolite eruption from heterogeneous hot zones embedded within a cool, shallow magma reservoir. *Journal of Geophysical Research: Solid Earth*, *124*, 1–19. https://doi.org/10.1029/2018JB016418

Andersen, N. L., Singer, B. S., Costa, F., Fournelle, J., Herrin, J. S., & Fabbro, G. N. (2018). Petrochronologic perspective on rhyolite volcano unrest at Laguna del Maule Chile. *Earth and Planetary Science Letters*, *493*, 57–70. https://doi.org/10.1016/j.epsl.2018.03.043

Andersen, N. L., Singer, B. S., Jicha, B. R., Beard, B. L., Johnson, C. M., & Licciardi, J. M. (2017). Pleistocene to Holocene growth of a large upper crustal rhyolitic magma reservoir beneath the active Laguna del Maule volcanic field, central Chile. *Journal of Petrology*, *58*, 85–114. https://doi.org/10.1093/petrology/egx006

Annen, C., Blundy, J. D., Leuthold, J., & Sparks, R. S. J. (2015). Construction and evolution of igneous bodies: Towards an integrated perspective of crustal magmatism. *Lithos*, *230*, 206–221. https://doi.org/10.1016/j.lithos.2015.05.008

Árnason, K., Vilhjálmsson, A. M., & Bjornsdottir, T. (2007). *A Study of the Krafla Volcano Using Gravity, Micro Earthquake and MT Data, in: Short Course II on Surface Exploration for Geothermal Resources* (pp. 1–14). Kenya: Lake Naivasha.

Baba, K., Chave, A. D., Evans, R. L., Hirth, G., & Mackie, R. L. (2006). Mantle dynamics beneath the East Pacific Rise at 17°S: Insights from the Mantle Electromagnetic and Tomography (MELT) experiment. *Journal of Geophysical Research*, *111*, 1–18. https://doi.org/10.1029/2004JB003598

Bachmann, O., & Huber, C. (2016). Silicic magma reservoirs in the Earth's crust. *American Mineralogist*, *101*, 2377–2404. https://doi.org/10.2138/am-2016-5675

Bai, T., Thurber, C., Lanza, F., Singer, B. S., & Cardona, C. (2020). Teleseismic tomography of the Laguna del Maule volcanic field in Chile. *Journal of Geophysical Research: Solid Earth*, *25*, e2020JB019449. https://doi.org/10.1029/2020JB019449

Bato, M. G., Pinel, V., Yan, Y., Jouanne, F., & Vandemeulebrouck, J. (2018). Possible deep connection between volcanic systems evidenced by sequential assimilation of geodetic data. *Scientific Reports*, *8*(1), 1–13. https://doi.org/10.1038/s41598-018-29811-x

Becken, M., Ritter, O., & Burkhardt, H. (2008). Mode separation of magnetotelluric responses in three-dimensional environments. *Geophysical Journal International*, *172*, 67–86. https://doi.org/10.1111/j.1365-246X.2007.03612.x

Bedrosian, P. A. (2007). MT +, integrating magnetotellurics to determine Earth structure, physical state, and processes. *Surveys in Geophysics*, *28*, 121–167. https://doi.org/10.1007/s10712-007-9019-6

Benavente, O. M., Tassi, F., Reich, M., Aguilera, F., Capecchiacci, F., Gutiérrez, F., et al. (2016). Chemical and isotopic features of cold and thermal fluids discharged in the Southern Volcanic Zone between 32.5°S and 36°S: Insights into the physical and chemical processes controlling fluid geochemistry in geothermal systems of Central Chile. *Chemical Geology*, *420*, 97–113. https://doi.org/10.1016/j.chemgeo.2015.11.010

Brothelande, E., Amelung, F., Yunjun, Z., & Wdowinski, S. (2018). Geodetic evidence for interconnectivity between Aira and Kirishima magmatic systems. *Japan Scientific Report*, *8*(1), 1–10. https://doi.org/10.1038/s41598-018-28026-4

Burd, A. I., Booker, J. R., Mackie, R., Favetto, A., & Pomposiello, M. C. (2014). Three-dimensional electrical conductivity in the mantle beneath the Payún Matrú Volcanic Field in the Andean backarc of Argentina near 36.5 S: Evidence for decapitation of a mantle plume by resurgent upper mantle shear during slab steepening. *Geophysical Journal International*, *198*, 812–827. https://doi.org/10.1093/gji/ggu145

Cardona, C., Tassara, A., Gil-cruz, F., Lara, L., Morales, S., Kohler, P., & Franco, L. (2018). Crustal seismicity associated to rapid surface uplift at Laguna del Maule Volcanic Complex Southern Volcanic Zone of the Andes. *Journal of Volcanology and Geothermal Research*. https://doi.org/10.1016/j.jvolgeores.2018.01.009

Cashman, K. V., Sparks, R. S. J., & Blundy, J. D. (2017). Vertically extensive and unstable magmatic systems: A unified view of igneous processes. *Science*, *(80)*, 355, eaag3055. https://doi.org/10.1126/science.aag3055

Chave, A. D., & Jones, A. G. (2012). *The Magnetotelluric Method—Theory and Practice*. Cambridge, UK: Cambridge Unviersity Press.

Comeau, M. J., Unsworth, M. J., & Cordell, D. (2016). New constraints on the magma distribution and composition beneath Volcán Uturuncu and the southern Bolivian Altiplano from magnetotelluric data. *Geosphere*, *12*, 1391–1421. https://doi.org/10.1130/GES01277.1

Constable, S., Parker, R. L., & Constable, C. (1987). Occam's inversion: A practical algorithm for generating smooth models from electromagnetic sounding data. *Geophysics*, *52*, 289–300. https://doi.org/10.1190/1.1442303

Cook, F. A., & Jones, A. G. (1995). Seismic reflections and electrical conductivity: A case of Holmes's curious dog? *Geology*, *23*, 141–144. https://doi.org/10.1130/0091-7613(1995)023<0141:sraeca>2.3.co;2

Cordell, D., Unsworth, M. J., & Díaz, D. (2018). Imaging the Laguna del Maule volcanic field, central Chile using magnetotellurics: Evidence for crustal melt regions laterally-offset from surface vents and lava flows. *Earth and Planetary Science Letters*, *488*, 168–180. https://doi.org/10.1016/j.epsl.2018.01.007

Cruden, A., & Weinberg, R. F. (2018). Mechanisms of magma transport and storage in the lower and middle crust—Magma segregation, ascent and emplacement. In *Volcanic and Igneous Plumbing Systems* (pp. 13–53). Elsevier Inc. https://doi.org/10.1016/B978-0-12-809749-6/00002-9

Díaz, D., Zuñiga, F., & Castruccio, A. (2020). The interaction between active crustal faults and volcanism: A case study of the Liquiñe-Ofqui Fault Zone and Osorno volcano, southern Andes, using magnetotellurics. *Journal of Volcanology and Geothermal Research*, *393*, 106806. https://doi.org/10.1016/j.jvolgeores.2020.106806

Egbert, G. D., & Kelbert, A. (2012). Computational recipes for electromagnetic inverse problems. *Geophysical Journal International*, *189*, 251–267. https://doi.org/10.1111/j.1365-246X.2011.05347.x

Feigl, K. L., Le Mével, H., Tabrez Ali, S., Cordova, L., Andersen, N. L., DeMets, C., & Singer, B. S. (2014). Rapid uplift in Laguna del Maule volcanic field of the Andean southern volcanic zone (Chile) 2007–2012. *Geophysical Journal International*, *196*, 885–901. https://doi.org/10.1093/gji/ggt438

Fisher, R. A. (1925). *Statistical Methods for Research Workers, Annals of Applied Biology*. London, UK: Oliver and Boyd. https://doi.org/10.1111/j.1744-7348.1926.tb04258.x

García-Yeguas, A., Ledo, J., Piña-Varas, P., Prudencio, J., Queralt, P., Marcuello, A., et al. (2017). A 3D joint interpretation of magnetotelluric and seismic tomographic models: The case of the volcanic island of Tenerife. *Computational Geosciences*, *109*, 95–105. https://doi.org/10.1016/j.cageo.2017.08.003

Garibaldi, N., Tikoff, B., Peterson, D., Davis, J. R., & Keranen, K. (2020). Statistical separation of tectonic and inflation-driven components of deformation on silicic reservoirs, Laguna del Maule volcanic field Chile. *Journal of Volcanology and Geothermal Research*, *389*, 106744. https://doi.org/10.1016/j.jvolgeores.2019.106744

Glover, P. W. J., Hole, M. J., & Pous, J. (2000). A modified Archie's law for two conducting phases. *Earth and Planetary Science Letters*, *180*, 369–383. https://doi.org/10.1016/S0012-821X(00)00168-0

Guo, X., Zhang, L., Behrens, H., & Ni, H. (2016). Probing the status of felsic magma reservoirs: Constraints from the P-T-H2O dependences of electrical conductivity of rhyolitic melt. *Earth and Planetary Science Letters*, *433*, 54–62. https://doi.org/10.1016/j.epsl.2015.10.036

Hildreth, W., Godoy, E., Fierstein, J., & Singer, B. S. (2010). Laguna del Maule volcanic field: Eruptive history of a Quaternary basalt-to-rhyolite distributed volcanic field on the Andean range crest in central Chile. In *Servicio Nacional de Geología y Minería Chile* (Vol. Boletín 63, p. 142). Santiago, Chile: Servicio Nacional de Geología y Minería.

Hill, G. J., Caldwell, T. G., Heise, W., Chertkoff, D. G., Bibby, H. M., Burgess, M. K., et al. (2009). Distribution of melt beneath Mount St Helens and Mount Adams inferred from magnetotelluric data. *Nature Geoscience*, *2*, 785–789. https://doi.org/10.1038/ngeo661

Iyer, H. (1984). Geophysical evidence for the locations, shapes and sizes, and internal structures of magma chambers beneath regions of quaternary volcanism. *Philosophical Transactions of the Royal Society A - Mathematical Physical and Engineering Sciences*, *310*, 473–510. https://doi.org/10.1098/rsta.1984.0005

Jiracek, G. R., Gustafson, E. P., & Mitchell, P. S. (1983). Magnetotelluric results opposing magma origin of crustal conductors in the Rio Grande Rift. *Tectonophysics*, *94*, 299–326. https://doi.org/10.1016/0040-1951(83)90022-7

Kalscheuer, T., Juanatey, M. A. G., Meqbel, N., & Pedersen, L. B. (2010). Non-linear model error and resolution properties from two-dimensional single and joint inversions of direct current resistivity and radiomagnetotelluric data. *Geophysical Journal International*, *182*, 1174–1188. https://doi.org/10.1111/j.1365-246X.2010.04686.x

Kelbert, A., Egbert, G. D., & DeGroot-Hedlin, C. (2012). Crust and upper mantle electrical conductivity beneath the Yellowstone Hotspot Track. *Geology*, *40*, 447–450. https://doi.org/10.1130/G32655.1

Kelbert, A., Meqbel, N., Egbert, G., & Tandon, K. (2014). ModEM: A modular system for inversion of electromagnetic geophysical data. *Computational Geosciences*, *66*, 40–53. https://doi.org/10.1016/j.cageo.2014.01.010

Klug, J. D., Singer, B. S., Kita, N. T., & Spicuzza, M. J. (2020). Storage and evolution of Laguna del Maule rhyolites: Insight from volatile and trace element contents in melt inclusions. *Journal of Geophysical Research: Solid Earth*, *125*, e2020JB019475. https://doi.org/10.1029/2020JB019475

Klügel, A., Longpré, M. A., García-Cañada, L., & Stix, J. (2015). Deep intrusions, lateral magma transport and related uplift at ocean island volcanoes. *Earth and Planetary Science Letters*, *431*, 140–149. https://doi.org/10.1016/j.epsl.2015.09.031

Laumonier, M., Gaillard, F., Muir, D., Blundy, J. D., & Unsworth, M. J. (2017). Giant magmatic water reservoirs at mid-crustal depth inferred from electrical conductivity and the growth of the continental crust. *Earth and Planetary Science Letters*, *457*, 173–180. https://doi.org/10.1016/j.epsl.2016.10.023

Le Mével, H., Feigl, K. L., Córdova, L., DeMets, C., & Lundgren, P. (2015). Evolution of unrest at Laguna del Maule volcanic field (Chile) from InSAR and GPS measurements, 2003 to 2014. *Geophysical Research Letters*, *42*, 6590–6598. https://doi.org/10.1002/2015GL064665

Lee, B., Unsworth, M. J., Arnason, K., & Cordell, D. (2020). Imaging the magmatic system beneath the Krafla geothermal field, Iceland: A new 3-D electrical resistivity model from inversion of magnetotelluric data. *Geophysical Journal International*, *220*, 541–567. https://doi.org/10.1093/gji/ggz427

Lees, J. M. (2007). Seismic tomography of magmatic systems. *Journal of Volcanology and Geothermal Research*, *167*, 37–56. https://doi.org/10.1016/j.jvolgeores.2007.06.008

Lerner, A. H., O'Hara, D., Karlstrom, L., Ebmeier, S. K., Anderson, K. R., & Hurwitz, S. (2020). The prevalence and significance of offset magma reservoirs at arc volcanoes. *Geophysical Research Letters*, *47*, e2020GL087856. https://doi.org/10.1029/2020GL087856

Lowenstern, J. B., Sisson, T. W., & Hurwitz, S. (2017). *Probing Magma Reservoirs to Improve Volcano Forecasts* (pp. 1–9). Washington. DC: Eos. https://doi.org/10.1029/2017EO085189

Magee, C., Stevenson, C. T. E., Ebmeier, S. K., Keir, D., Hammond, J. O. S., Gottsmann, J. H., et al. (2018). Magma plumbing systems: A geophysical perspective. *Journal of Petrology*, *0*, 1–35. https://doi.org/10.1093/petrology/egy064

Massey, F. J. (1951). The Kolmogorov-Smirnov test for goodness of fit. *Journal of the American Statistical Association*, *46*(253), 68–78.

Masterlark, T., Haney, M., Dickinson, H., Fournier, T., & Searcy, C. (2010). Rheologic and structural controls on the deformation of Okmok volcano, Alaska: FEMs, InSAR, and ambient noise tomography. *Journal of Geophysical Research*, *115*, B02409. https://doi.org/10.1029/2009JB006324

McGary, R., Evans, R., & Wannamaker, P. E. (2014). Pathway from subducting slab to surface for melt and fluids beneath Mount Rainier. *Nature*, *511*(7509), 338–340. https://doi.org/10.1038/nature13493

Meju, M. A. (2009). Regularized extremal bounds analysis (REBA): An approach to quantifying uncertainty in nonlinear geophysical inverse problems. *Geophysical Research Letters*, *36*, 1–5. https://doi.org/10.1029/2008GL036407

Miensopust, M. P. (2017). Application of 3-D EM inversion in practice: Challenges pitfalls and solution approaches. *Surveys in Geophysics*, *38*(5), 869–933. https://doi.org/10.1007/s10712-017-9435-1

Miller, C. A., Le Mével, H., Currenti, G., Williams-Jones, G., & Tikoff, B. (2017). Microgravity changes at the Laguna del Maule volcanic field: Magma-induced stress changes facilitate mass addition. *Journal of Geophysical Research: Solid Earth*, *122*, 3179–3196. https://doi.org/10.1002/2017JB014048

Miller, C. A., Williams-Jones, G., Fournier, D., & Witter, J. (2017). 3D gravity inversion and thermodynamic modelling reveal properties of shallow silicic magma reservoir beneath Laguna del Maule Chile. *Earth and Planetary Science Letters*, *459*, 14–27. https://doi.org/10.1016/j.epsl.2016.11.007

Miller, R. L., & Kahn, J. S. (1962). *Statistical Analysis in the Geological Sciences*. Ltd, New York: John Wiley & Sons.

Moorkamp, M. (2017). Integrating electromagnetic data with other geophysical observations for enhanced imaging of the earth: A tutorial and review. *Surveys in Geophysics*, *38*(5), 935–962. https://doi.org/10.1007/s10712-017-9413-7

Muñoz, G., & Rath, V. (2006). Beyond smooth inversion: The use of nullspace projection for the exploration of non-uniqueness in MT. *Geophysical Journal International*, *164*, 301–311. https://doi.org/10.1111/j.1365-246X.2005.02825.x

Ogawa, Y., Ichiki, M., Kanda, W., Mishina, M., & Asamori, K. (2014). Three-dimensional magnetotelluric imaging of crustal fluids and seismicity around Naruko volcano NE Japan. *Earth, Planets and Space*, *66*, 1–13.

Parker, R. L. (1994). *Geophysical Inverse Theory*. Princeton, NJ: Princeton University Press.

Peterson, D. E., Garibaldi, N., Keranen, K., Tikoff, B., Miller, C., Lara, L. E., et al. (2020). Active normal faulting, diking, and doming above the rapidly inflating Laguna del Maule volcanic field, Chile, imaged with CHIRP, magnetic, and focal mechanism data. *Journal of Geophysical Research: Solid Earth*, *125*, e2019JB019329. https://doi.org/10.1029/2019JB019329

Piña-Varas, P., Ledo, J., Queralt, P., Marcuello, A., & Perez, N. (2018). On the detectability of Teide volcano magma chambers (Tenerife, Canary Islands) with magnetotelluric data. *Earth, Planets and Space*, *70*(1), 1–11. https://doi.org/10.1186/s40623-018-0783-y

Pinel, V., & Jaupart, C. (2004). Magma storage and horizontal dyke injection beneath a volcanic edifice. *Earth and Planetary Science Letters*, *221*, 245–262. https://doi.org/10.1016/S0012-821X(04)00076-7

Pommier, A. (2014). Interpretation of magnetotelluric results using laboratory measurements. *Surveys in Geophysics*, *35*, 41–84. https://doi.org/10.1007/s10712-013-9226-2

Pritchard, M. E., de Silva, S. L., Michelfelder, G., Zandt, G., Mcnutt, S. R., Gottsmann, J., et al. (2018). Synthesis: PLUTONS: Investigating the relationship between pluton growth and volcanism in the Central Andes. *Geosphere*, *14*, 954–982. https://doi.org/10.1130/GES01578.1

Pritchard, M. E., & Gregg, P. M. (2016). Geophysical evidence for silicic crustal melt in the continents: Where, what kind, and how much? *Elements*, *12*, 121–127. https://doi.org/10.2113/gselements.12.2.121

Robertson, K., Thiel, S., & Meqbel, N. (2020). Quality over quantity: On workflow and model space exploration of 3D inversion of MT data. *Earth, Planets and Space*, *72*(1), 1–22. https://doi.org/10.1186/s40623-019-1125-4

Sanders, C. O., Ponko, S. C., Nixon, L. D., & Schwartz, E. A. (1995). Seismological evidence for magmatic and hydrothermal structure in Long Valley caldera from local earthquake attenuation and velocity tomography. *Journal of Geophysical Research*, *100*, 8311–8326. https://doi.org/10.1029/95JB00152

Schmandt, B., Jiang, C., & Farrell, J. (2019). Seismic perspectives from the western U.S. on magma reservoirs underlying large silicic calderas. *Journal of Volcanology and Geothermal Research*, *384*, 158–178. https://doi.org/10.1016/j.jvolgeores.2019.07.015

Schnaidt, S., & Heinson, G. (2015). Bootstrap resampling as a tool for uncertainty analysis in 2-D magnetotelluric inversion modelling. *Geophysical Journal International*, *203*, 92–106. https://doi.org/10.1093/gji/ggv264

Sorey, M. L., Evans, W. C., Kennedy, B. M., Farrar, C. D., Hainsworth, L. J., & Hausback, B. (1998). Carbon dioxide and helium emissions from a reservoir of magmatic gas beneath Mammoth Mountain, California. *Journal of Geophysical Research*, *103*, 15,303–15,323. https://doi.org/10.1029/98JB01389

Sparks, R. S. J., Annen, C., Blundy, J. D., Cashman, K. V., Rust, A. C., & Jackson, M. D. (2019). Formation and dynamics of magma reservoirs. *Philosophical Transactions of the Royal Society A - Mathematical Physical and Engineering Sciences*, *377*, 1–30. https://doi.org/10.1098/rsta.2018.0019

Stanley, W. D., & Blakely, R. J. (1995). The Geysers-Clear Lake geothermal area, California—An updated geophysical perspective of heat sources. *Geothermics*, *24*, 187–221. https://doi.org/10.1016/0375-6505(94)00048-h

Szymanowski, D., Wotzlaw, J., Ellis, B. S., Bachmann, O., Guillong, M., & von Quadt, A. (2017). Protracted near-solidus storage and pre-eruptive rejuvenation of large magma reservoirs. *Nature Geoscience*, *10*(10), 777–782. https://doi.org/10.1038/NGEO3020

Thiel, S., & Heinson, G. (2010). Crustal imaging of a mobile belt using magnetotellurics: An example of the Fowler Domain in South Australia. *Journal of Geophysical Research*, *115*, 1–18. https://doi.org/10.1029/2009JB006698

Unsworth, M. J., & Rondenay, S. (2013). Mapping the distribution of fluids in the crust and lithospheric mantle utilizing geophysical methods. In D. E. Harlov, & H. Austrheim (Eds.), *Metasomatism and the Chemical Transformation of Rock* (pp. 535–598). Berlin Heidelberg, Berlin, Germany: Springer. https://doi.org/10.1007/978-3-642-28394-9

Wespestad, C. E., Thurber, C. H., Andersen, N. L., Singer, B. S., Cardona, C., Zeng, X., et al. (2019). Magma reservoir below Laguna del Maule volcanic field, Chile, imaged with surface-wave tomography. *Journal of Geophysical Research: Solid Earth*, *124*, 2858–2872. https://doi.org/10.1029/2018JB016485

Zellmer, G. F., & Annen, C. (2008). An introduction to magma dynamics. *Geological Society of London*, *304*, 1–13. https://doi.org/10.1144/SP304.1

Zhan, Y., Gregg, P. M., le Mével, H., Miller, C. A., & Cardona, C. (2019). Integrating reservoir dynamics, crustal stress, and geophysical observations of the Laguna del Maule magmatic system by FEM models and data assimilation. *Journal of Geophysical Research: Solid Earth*, *124*, 13,547–13,562. https://doi.org/10.1029/2019JB018681